

# Large contribution of natural aerosols to uncertainty in indirect forcing

K. S. Carslaw<sup>1</sup>, L. A. Lee<sup>1</sup>, C. L. Reddington<sup>1</sup>, K. J. Pringle<sup>1</sup>, A. Rap<sup>1</sup>, P. M. Forster<sup>1</sup>, G. W. Mann<sup>1,2</sup>, D. V. Spracklen<sup>1</sup>, M. T. Woodhouse<sup>1,†</sup>, L. A. Regayre<sup>1</sup> & J. R. Pierce<sup>3</sup>

**The effect of anthropogenic aerosols on cloud droplet concentrations and radiative properties is the source of one of the largest uncertainties in the radiative forcing of climate over the industrial period. This uncertainty affects our ability to estimate how sensitive the climate is to greenhouse gas emissions. Here we perform a sensitivity analysis on a global model to quantify the uncertainty in cloud radiative forcing over the industrial period caused by uncertainties in aerosol emissions and processes. Our results show that 45 per cent of the variance of aerosol forcing since about 1750 arises from uncertainties in natural emissions of volcanic sulphur dioxide, marine dimethylsulphide, biogenic volatile organic carbon, biomass burning and sea spray. Only 34 per cent of the variance is associated with anthropogenic emissions. The results point to the importance of understanding pristine pre-industrial-like environments, with natural aerosols only, and suggest that improved measurements and evaluation of simulated aerosols in polluted present-day conditions will not necessarily result in commensurate reductions in the uncertainty of forcing estimates.**

The impact of aerosol changes on cloud albedo (called the aerosol first indirect forcing)<sup>1</sup> is estimated<sup>2</sup> to exert a global mean radiative forcing of climate over the industrial period between  $-0.4 \text{ W m}^{-2}$  and  $-1.8 \text{ W m}^{-2}$ . Other aerosol–cloud interaction effects, involving rapid adjustments, may be of comparable magnitude<sup>3</sup> but their radiative effects are even less well understood on a global scale<sup>3,4</sup>. The uncertainty in the aerosol forcing is much larger than the uncertainty in the well-constrained positive forcing of  $1.7 \pm 0.2 \text{ W m}^{-2}$  that is due to carbon dioxide change. The aerosol indirect forcing therefore has a highly uncertain influence on climate change and has the potential to mask a significant portion of greenhouse gas warming<sup>5</sup>.

The magnitude of the forcing caused by aerosol–cloud interactions depends on several poorly modelled aspects of the climate, but is broadly understood to stem from different treatments of aerosols, clouds and radiation<sup>3,6–8</sup>. Nevertheless, the fundamental driver is the change in aerosols from the pre-industrial period to the present day, which controls the change in cloud droplet concentrations. It is recognized that quantification of aerosol indirect forcing requires an understanding of both the pre-industrial aerosol state<sup>9–12</sup> and the effect of the substantial anthropogenic perturbation. However, because of the complexity of processes that determine cloud-forming aerosol concentrations<sup>10</sup> and the computational expense of global aerosol models which explicitly simulate their production and loss processes<sup>13–16</sup>, a comprehensive assessment of the magnitude and leading causes of uncertainty in indirect forcing has not been attempted.

## Perturbed parameter simulations

Here we carry out a variance-based sensitivity analysis of a global aerosol model to attribute the uncertainty in the aerosol first indirect forcing to uncertainties in the emissions and processes that control changes in aerosol over the industrial period. We perform an ensemble of perturbed parameter global aerosol microphysical model simulations using present-day (PD) and pre-industrial (PI) emissions (PD is defined as the year 2000 and PI is defined<sup>17</sup> as 1750, with additional PI simulations to test the effect of using alternative reference years of 1850 or 1900). The 168

1-year model simulations in the PI and PD periods cover the full expert-elicited uncertainty space of 28 parameters describing natural and anthropogenic aerosol emissions, aerosol precursor gas emissions, microphysical processes and structures of the aerosol model (see Methods). To characterize fully the magnitude and causes of model uncertainty we use Bayesian emulators conditioned on the ensemble data to generate continuous model output across the parameter space<sup>18,19</sup>. This approach enables a Monte Carlo sampling of the model uncertainty space<sup>20</sup> so that a full variance-based sensitivity analysis of the model outputs can be performed.

## Radiative forcing uncertainty

Figure 1 shows the annual mean first indirect radiative forcing and the associated  $1\sigma$  uncertainty when assuming the 1750 reference state. The global annual mean indirect forcing is  $-1.16 \text{ W m}^{-2}$  ( $\sigma = 0.22 \text{ W m}^{-2}$ , 95% confidence interval  $-0.7 \text{ W m}^{-2}$  to  $-1.6 \text{ W m}^{-2}$ ), compared to the multi-model range reported in ref. 2 of  $-0.4 \text{ W m}^{-2}$  to  $-1.8 \text{ W m}^{-2}$  (best estimate,  $-0.7 \text{ W m}^{-2}$ ) and an estimate ( $-0.6 \pm 0.4 \text{ W m}^{-2}$ ) based on assimilated PD aerosol optical depth<sup>21</sup>. Our estimated 95% confidence interval is slightly narrower than the multi-model ensemble range, most probably because the latter includes structural differences in the host model aerosol, cloud and radiation schemes<sup>2,3,6</sup>. Nevertheless, improved understanding of the aerosol processes and emissions would clearly help to reduce uncertainty in model forcing calculations.

The seasonal variation of global mean forcing and the contributions of different parameters to the uncertainty are shown in Fig. 2a and b (see the Methods and Extended Data Table 3 for the definition and elicited range of each parameter). The eight most important parameters account for 92% of the forcing variance: volcanic  $\text{SO}_2$  emissions, anthropogenic  $\text{SO}_2$  emissions, dimethyl sulphide (DMS) emissions from marine biota, the width of the accumulation mode, dry deposition of accumulation mode aerosol, sub-grid sulphate particle formation, the width of the Aitken mode, and the diameter of emitted fossil fuel combustion particles. Several parameters that have a large effect on uncertainties in PD concentrations of cloud condensation nuclei (CCN)<sup>18</sup>

<sup>1</sup>School of Earth and Environment, University of Leeds, Leeds, LS2 9JT, UK. <sup>2</sup>National Centre for Atmospheric Science, University of Leeds, Leeds, LS2 9JT, UK. <sup>3</sup>Department of Atmospheric Science, Colorado State University, Fort Collins, Colorado 80523, USA. <sup>†</sup>Present address: CSIRO Marine and Atmospheric Research, Aspendale, Victoria 3195, Australia.

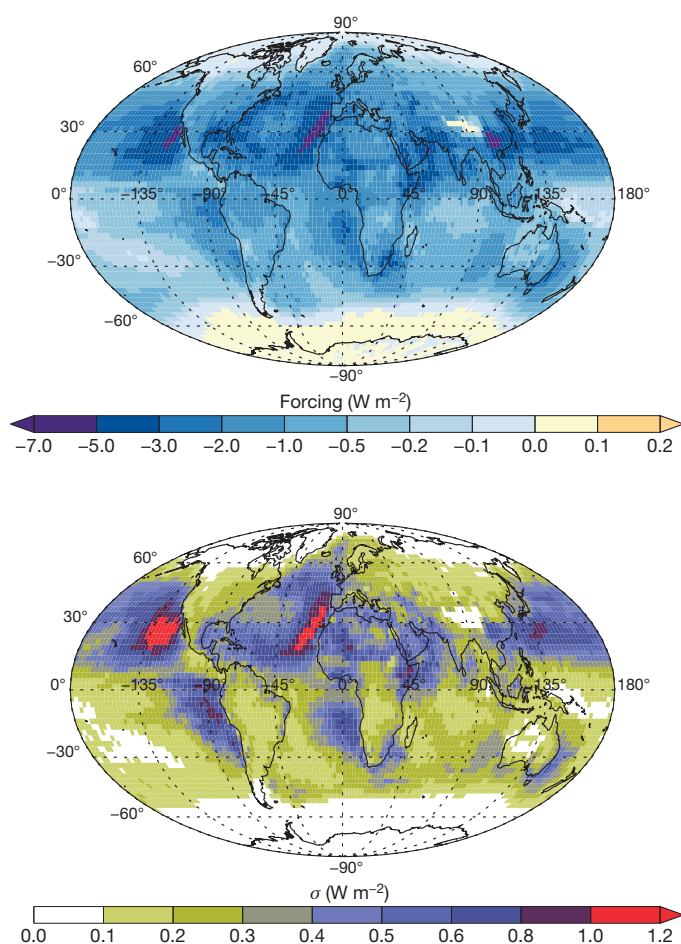


**Figure 1 | The global distribution of annual mean aerosol first indirect forcing and associated uncertainty.** a, First indirect forcing; b, standard deviation  $\sigma$  of forcing. The maps were computed from a Monte Carlo sampling of an emulator of forcing in each grid cell of the model.

have a small effect on forcing uncertainty, which is related to the way they perturb PI and PD CCN, as we discuss below.

A striking aspect of the results is the large contribution to the global mean forcing uncertainty from emissions of natural aerosol and precursor gases. Together, emissions of volcanic  $\text{SO}_2$ , marine DMS, biogenic volatile organic carbon (forming secondary organic aerosol), biomass burning and sea spray account for 45% of the global annual mean forcing variance (Fig. 2b). This compares with 34% of the annual mean forcing variance that is due to the eight parameters associated with anthropogenic fossil fuel, biofuel,  $\text{SO}_2$  and sulphate particle emissions. The biomass burning emissions were perturbed as a single parameter and not separated into natural wildfires and anthropogenic biomass burning. However, the annual mean 2% contribution of biomass burning to the forcing variance means that the natural–anthropogenic split is not important to our overall conclusions. Moreover, the seasonality of the uncertainty caused by biomass burning suggests that it can be attributed mostly to northern mid-latitude emissions associated with natural fires (see Methods).

The relative contribution of different parameters to the uncertainty depends on the sampled range in the ensemble (Extended Data Table 3). The range for DMS (−50%/+100%) is consistent with assessments of multiple emission parameterizations<sup>22</sup> and the same range for volcanic  $\text{SO}_2$  is plausible given the uncertainty in sources<sup>23</sup>. However, our assumed range of −40%/+50% for the main anthropogenic aerosol uncertainty ( $\text{SO}_2$  emissions) is high compared to the most recent inventories. Thus, it is likely that our estimate of the natural aerosol effect on forcing uncertainty is an underestimate.

It is important to note that most of the natural emissions do not, by themselves, cause a forcing over the industrial period because the emission source strengths were defined to be the same in the PI and PD simulations (except for biomass burning); that is, a high setting of the emissions in the PI simulation was paired with the same high setting in the PD. However, natural emissions affect the uncertainty in the aerosol first indirect forcing because they affect the background aerosol state upon which the forcing is calculated (see below).

Because our variance-based approach considers parameter interactions, we are able to establish that the large contribution of natural aerosol emissions to forcing uncertainty is not strongly dependent on the magnitude of the other parameters. This is important information because, for example, the large sensitivity of forcing to natural sulphur emissions could be overemphasized if particle formation rates due to sulphuric-acid-driven nucleation were too high in the model. However, such parameter interactions can be quantified as the difference between the sum of the main effect variances (coloured bars in Fig. 2b) and the total variance (100% in Fig. 2b); see the Methods. Interactions generally account for less than 10% of the total forcing variance, demonstrating that the ranked uncertainty results are robust to uncertainties in the model set-up.

The effect of some parameters on forcing uncertainty could be underestimated if the parameter varied in an unknown way between the PI and PD eras, which we have not accounted for here. For example, if DMS or volcanic emissions were at the low end of the uncertainty range in the PI and at the higher end in the PD then the resulting increase in sulphate aerosol over this period would constitute an additional uncertainty in the forcing<sup>23</sup>. It is plausible that natural emissions change over time, implying that the uncertainty attributable to these parameters could be underestimated. Whether other parameters behave in this way depends on the extent to which the model processes represent an absolute understanding or whether they have been inadvertently tuned to conditions in the PD atmosphere.

### Alternative reference years

The contribution of natural emissions to the forcing uncertainty will depend on the reference year that is used. The 1750 reference, used here, is commonly assumed to represent a pristine PI state, whereas early industrial decades from the 1850s onwards have also been used<sup>24</sup>. To test the effect of using alternative years for forcing, we repeated our calculations for the periods 1850–2000, 1850–1980 and 1900–2000 (limited to June to reduce computational cost). For the alternative reference years we used the same natural emissions as in 1750, but different anthropogenic emissions (see Methods). As expected, the indirect forcing is lower when a slightly polluted reference year is used (a June mean of  $-1.30 \text{ W m}^{-2}$  for 1850 and  $-0.96 \text{ W m}^{-2}$  for 1900, versus  $-1.42 \text{ W m}^{-2}$  for 1750). The uncertainty analysis shows that the standard deviation of forcing is slightly larger when the reference year is 1850 ( $\sigma = 21\%$  of mean) than for 1750 ( $\sigma = 19\%$  of mean); see Extended Data Table 4. However, the uncertainties in 1850 emissions are likely to be larger than for the year 2000, which we have not attempted to account for, so we expect our estimate of 1850–2000 forcing uncertainty to be an underestimate. The contribution of anthropogenic emissions to the forcing uncertainty is also greater using an 1850 reference (46% of variance, versus 38% using 1750). This change compared to 1750 is mainly caused by the increased contribution from fossil fuel and sulphate particle emissions. These results show that natural emissions remain a substantial part of the forcing uncertainty even when slightly polluted reference years are used. They also confirm that the uncertainty in forcing is strongly sensitive to the assumed PI emissions, whether natural or anthropogenic: the large absolute change in anthropogenic emissions between 1980 and 2000 causes hardly any change in the contribution of anthropogenic emissions to the uncertainty in forcing referenced to 1850 (47% versus 46% of variance; see Extended Data Table 4), but the small absolute change in emissions

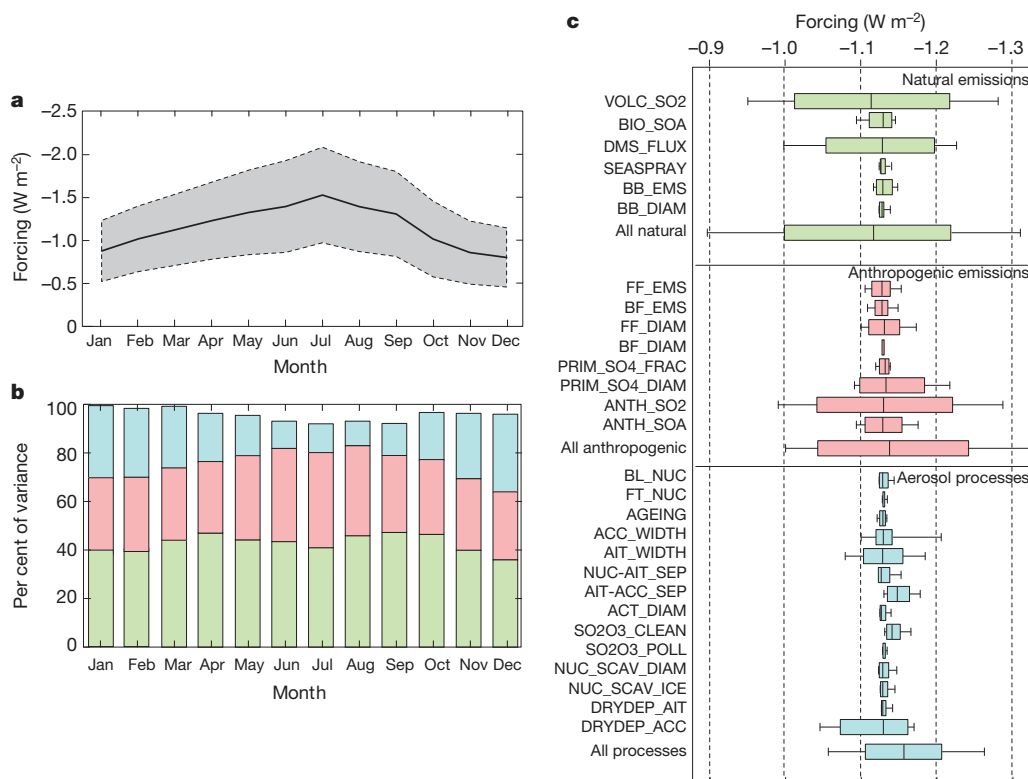


**Figure 2 | Magnitude and sources of uncertainty in global mean aerosol first indirect forcing.** **a**, Global mean forcing and two-standard-deviation uncertainty range. **b**, Seasonal cycle of the contribution of different groups of parameters to global monthly mean forcing variance (green, natural emissions; pink, anthropogenic emissions; blue, aerosol processes). The difference

between 1750 and 1850 causes a large change in the anthropogenic contribution (38% to 46%).

Although not a focus of this work, our results also suggest that most of the aerosol–cloud forcing has probably been realized by 1980 and has changed little between 1980 and 2000 (comparing 1850–1980 and 1850–2000 time periods; see Extended Data Table 4). This, combined with the uncertainty analysis, indicates that it may be possible to place a relatively tight constraint on the aerosol forcing over recent decades (compared to the PI-to-PD period), which would help determine the forcing contribution to the reduction in warming trend.

### Importance of natural aerosols

The large contribution of natural aerosol emissions to forcing uncertainty is caused by three factors (Fig. 3a–d). First, the  $1\sigma$  response of CCN to changing DMS emissions is 44% higher in the PI period than in the PD period ( $\sigma = 12.9 \text{ cm}^{-3}$  versus  $9.0 \text{ cm}^{-3}$ ) between  $60^\circ \text{ S}$  and  $60^\circ \text{ N}$  in July, caused by the more efficient nucleation of new particles in the cleaner PI atmosphere. Second, cloud droplet number concentrations increase more steeply with CCN when concentrations are low in the PI era. This effect occurs because high droplet concentrations limit the in-cloud supersaturation. Third, cloud albedo sensitivity to changes in cloud droplet concentrations (the susceptibility<sup>1</sup>) is higher in the PI era because the dependence of albedo  $A$  on droplet number  $N$  is approximately  $dA/dN = A(1 - A)/3N$ . The combined effect of these three factors means that the forcing uncertainty is more strongly affected by natural aerosol (which affects PI cloud albedo in a near-linear way) than PD anthropogenic aerosol (which affects PD albedo in a sub-linear way). For the region of high forcing off the coast of Chile, CCN concentrations rise in our model by a factor of 6.6 ( $75 \text{ cm}^{-3}$  in the PI period to  $500 \text{ cm}^{-3}$  in the PD). Under these conditions, and with a cloud albedo of 0.5, the sensitivity of albedo to CCN is about 15 times higher in the PI period than in the PD.

between the sum of variances and 100% is accounted for by parameter interactions. **c**, Global annual mean forcing uncertainty range due to specific parameters and groups of parameters. The box shows the interquartile range and the whisker shows the 9%–91% confidence interval. The definition of each parameter is given in Extended Data Table 3.

Although natural aerosol emissions cause only a small uncertainty in PI and PD CCN, they can have a disproportionate effect on forcing uncertainty compared to some process parameters, which we illustrate for typical conditions in Fig. 3e. For example, aerosol deposition processes were identified as a major uncertainty in PD CCN<sup>18</sup>. However, uncertainty in such a process causes an uncertainty in CCN that is in proportion to the aerosol abundance (so the absolute error in CCN will be higher in the PD than in the PI). In contrast, the uncertainty in DMS emissions causes approximately the same absolute error in CCN in the PI and PD. As shown in Fig. 3e, the relationship between CCN, cloud droplet concentrations and albedo means that there is some degree of cancellation of errors in the case where the CCN error is proportional to the amount of aerosol. For the illustrative conditions used in Fig. 3e, when PD CCN concentrations are about double the PI levels, the uncertainty in forcing is a factor of ten higher in the absolute case than in the proportional case.

### Implications

Our study provides the first assessment of how aerosol processes and emissions affect the uncertainty in indirect forcing between the PI and PD periods and provides quantitative support for previous studies that have highlighted the importance of understanding PI aerosol<sup>9–12</sup>. There are several implications. First, it will prove difficult to constrain the sources of forcing uncertainty by making observations in the PD atmosphere<sup>11,21</sup>, because the low sensitivity of PD clouds to these emissions<sup>18,22</sup> is unrepresentative of the PI atmosphere. We would need to understand the effects of natural emissions on PI-like aerosol. The nearest equivalent we have to PI conditions in the PD atmosphere is in very clean environments<sup>9</sup>, but the spread of perturbed particle concentrations<sup>10,25</sup> may make it difficult to observe sufficiently pristine environments, except over very remote marine locations<sup>26</sup>. Second, because the magnitude of the PI emissions themselves (notably volcanic and DMS) are now unmeasurable, some of the forcing uncertainty in

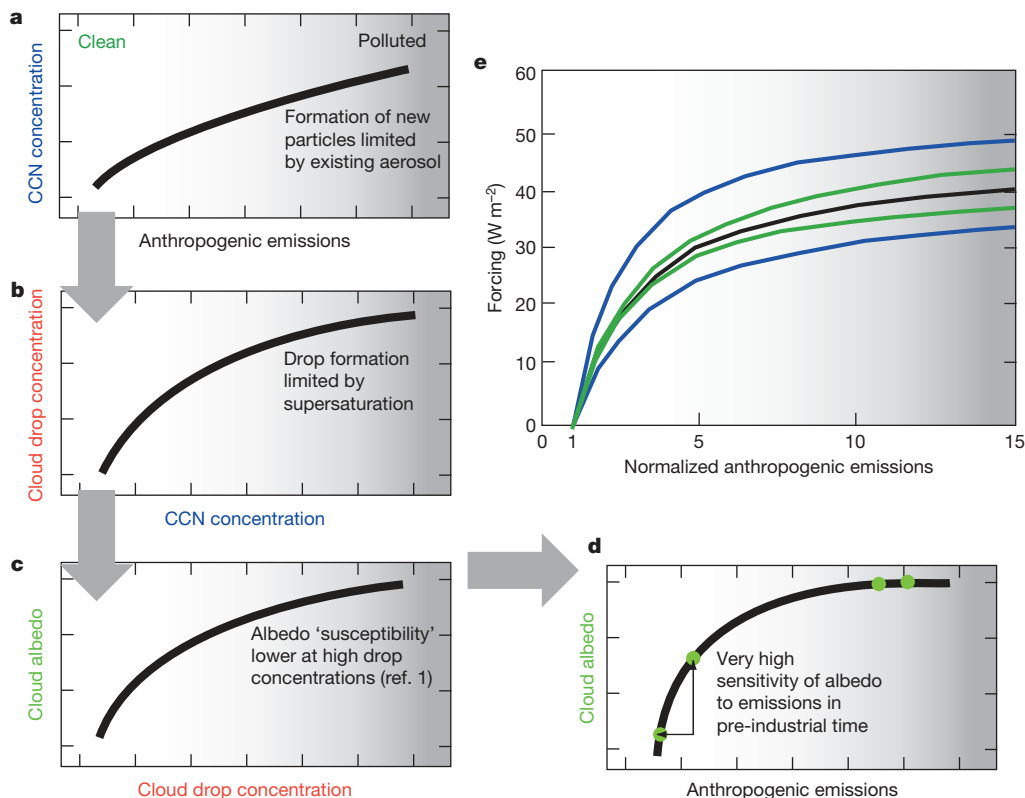


**Figure 3 | Schematic explaining the importance of natural emissions for forcing uncertainty.** **a**, CCN concentrations are more sensitive to emissions of sulphur precursor gases in the PI era because the condensation sink of the nucleating sulphuric acid vapour onto existing aerosol is lower. **b**, Cloud droplet concentrations are more sensitive to changes in CCN when droplet concentrations are low because higher droplet concentrations suppress in-cloud supersaturation and limit the activation of additional aerosol particles. **c**, Cloud albedo is more susceptible to changes in cloud droplet concentration when concentrations are low<sup>1</sup>. **d**, All three effects in **a–c** lead to a much higher sensitivity of albedo to precursor gas emissions in the PI era. **e**, Calculated effect of how the uncertainty in modelled aerosol affects the uncertainty in forcing. In this example, it is assumed that the CCN concentration scales in direct proportion with anthropogenic emissions (horizontal axis), as occurs approximately in the model. Uncertainties are then applied to CCN ( $\pm \Delta \text{CCN}$ ). The green lines show the uncertainty in forcing when  $\Delta \text{CCN}$  is proportional to the CCN concentration and the blue lines show a case where  $\Delta \text{CCN}$  is constant and independent of the anthropogenic emissions. The initial PI CCN concentration is  $50 \text{ cm}^{-3}$ , rising to a maximum of  $750 \text{ cm}^{-3}$  in the PD. The cloud droplet number concentration (CDNC) is

calculated as  $\text{CDNC} = 375 \times (1 - \exp(-0.0025 \times \text{CCN}))$  (ref. 28). The albedo  $A$  of the baseline cloud is assumed to be 0.5 and the albedo versus CDNC is  $dA/d\ln(\text{CDNC}) = A(1 - A)/3A$  (ref. 1). The forcing is calculated according to  $-F_0 T_a^2 \Delta A$ , where  $\Delta A$  is the change in albedo from the PI value (0.5),  $T_a$  is the transmission of the atmosphere (assumed to be 0.75) and  $F_0$  is the radiative flux, assumed to be  $340 \text{ W m}^{-2}$ . The black line shows the calculated forcing assuming the baseline aerosol number concentration. The green line shows the calculated forcing assuming  $\pm 30\%$  uncertainty in CCN ( $35\text{--}65 \text{ cm}^{-3}$  in the PI era to  $525\text{--}975 \text{ cm}^{-3}$  maximum in the PD). This calculation represents an uncertainty in aerosol concentrations due to a process that affects PI and polluted aerosol concentrations by the same factor, such as dry deposition. The blue line shows the calculated forcing assuming  $\pm 15 \text{ cm}^{-3}$  uncertainty in CCN ( $35\text{--}65 \text{ cm}^{-3}$  in the PI era, as in the scaled calculation, to a maximum polluted concentration of  $735\text{--}765 \text{ cm}^{-3}$ ). This calculation represents an uncertainty in aerosol concentrations due to a process or emission that affects PI and polluted aerosol by approximately the same absolute amount, such as caused by uncertainty in DMS or volcanic  $\text{SO}_2$  emissions. The small absolute change in aerosol has a much larger effect on forcing uncertainty than the scaled aerosol change.

climate simulations may be irreducible<sup>27</sup>. Therefore, empirical estimates of PI-to-PD forcing based on observations of aerosol and aerosol–cloud relations under PD conditions<sup>21,28</sup> may not be accurate. Third, efforts to constrain the magnitude of equilibrium climate sensitivity based on net forcing and ocean heat content relative to a PI reference<sup>24</sup> will always be hampered by our limited ability to constrain the natural aerosol state. Although it makes sense to define the forcing relative to a PI reference period when the forcing was zero and the Earth was approximately in energy balance, this does not imply zero error contribution from the reference state. We have shown that the uncertainties in PI-to-PD forcing are strongly affected by the PI aerosol. Other reference periods could be considered, but equilibrium climate sensitivity studies would need to account for uncertainties in ocean heat content. A final implication is that the major sources of uncertainty will depend on the period over which forcing is calculated, so future aerosol indirect forcing may be sensitive to a different set of parameters. Therefore, accurate simulation of past forcing, if this could be achieved, may not guarantee accurate future estimates. Furthermore, other aerosol–cloud interaction effects not considered here<sup>3,4</sup> may also

depend nonlinearly on aerosol between the PI period and the PD, and the uncertainties could be dominated by a different set of parameters.

Future efforts to reduce the uncertainty in simulated aerosol forcing need to combine measurements and models in ways that target sources of uncertainty, rather than relying on good model–observation agreement of PD aerosol as a measure of model fidelity. This means that models need to be based on sound microphysical processes and must not be reliant on tuning to PD aerosol levels. It is also essential for climate models and other models used for long-term simulations to include accurate representations of all natural aerosols, even if they have a small effect on PD aerosol levels in polluted environments. Even as future simulations of aerosol–cloud interaction become increasingly spatially resolved and able to capture more aerosol–cloud interaction processes and associated uncertainties, the uncertainty introduced from a poorly constrained pristine aerosol state will remain.

## METHODS SUMMARY

The GLObal Model of Aerosol Processes (GLOMAP)<sup>15,16</sup> calculates the time-dependent global distribution of size-resolved aerosol particles, including the



microphysical processes of particle nucleation, growth, coagulation, cloud cycling and deposition. The model transport is prescribed in terms of three-dimensional gridded wind speed, temperature and humidity fields from the European Centre for Medium-Range Weather Forecasts analyses. Anthropogenic emissions (from fossil fuel, biofuel and biomass burning) were set to their 1750 (plus alternative 1850 and 1900) values in the PI era and year 2000 values for the PD and were perturbed by a given factor (see Extended Data Tables 1 and 2). The uncertainty range for each parameter was chosen on the basis of expert elicitation<sup>18</sup>. The model was run for 168 combinations of parameter settings from among 28 parameters representing aerosol and precursor gas emissions, microphysical processes and aerosol model structures (see Extended Data Table 3).

The radiative forcing between the PI era and the PD was calculated using a radiative transfer model<sup>29</sup> and a monthly and geographically varying data set of cloud optical depth<sup>30</sup>. The diurnal cycle of incoming solar radiation was accounted for, but no diurnal cycle of cloud cover was assumed. Cloud droplet concentrations were calculated from the aerosol size distribution assuming a characteristic updraft speed of  $0.15 \text{ m s}^{-1}$  over ocean and  $0.3 \text{ m s}^{-1}$  over land. The albedo change in each grid cell was then calculated in terms of the change in cloud droplet effective radius at constant liquid water path<sup>31</sup>. Global mean forcings were calculated for 1750–2000, 1850–2000, 1900–2000 and 1850–1980 (see Extended Data Table 4).

A Gaussian process emulator was built to describe the monthly and global mean PI-to-PD change in top-of-the-atmosphere radiation across the space of the 28 uncertain parameters<sup>18</sup>, and then a Monte Carlo sampling of the emulator was used to generate a probability distribution of global mean forcing. Variance decomposition was used to quantify the fraction of variance attributable to the uncertain parameters. The forcing and uncertainty maps (Fig. 1) were generated by performing a similar analysis on separate emulators for each model grid cell.

**Online Content** Any additional Methods, Extended Data display items and Source Data are available in the online version of the paper; references unique to these sections appear only in the online paper.

Received 29 March; accepted 16 September 2013.

- Twomey, S. Aerosols, clouds, and radiation. *Atmos. Environ. A* **25**, 2435–2442 (1991).
- Forster, P. *et al.* in *Climate Change 2007: The Physical Science Basis, Contribution of Working Group I to the Fourth Assessment Report of the Intergovernmental Panel on Climate Change* (eds Solomon, S. *et al.*) 129–234 (Cambridge Univ. Press, 2007).
- Lohmann, U. & Feichter, J. Global indirect aerosol effects: a review. *Atmos. Chem. Phys.* **5**, 715–737 (2005).
- Stevens, B. & Feingold, G. Untangling aerosol effects on clouds and precipitation in a buffered system. *Nature* **461**, 607–613 (2009).
- Andreae, M. O., Jones, C. D. & Cox, P. J. Strong present-day aerosol cooling implies a hot future. *Nature* **435**, 1187–1190 (2005).
- Quaas, J. *et al.* Aerosol indirect effects—general circulation model intercomparison and evaluation with satellite data. *Atmos. Chem. Phys.* **9**, 8697–8717 (2009).
- Lohmann, U. & Ferrachat, S. Impact of parametric uncertainties on the present-day climate and on the anthropogenic aerosol effect. *Atmos. Chem. Phys.* **10**, 11373–11383 (2010).
- Pan, W. W., Tatang, M. A., McRae, G. J. & Prinn, R. G. Uncertainty analysis of indirect radiative forcing by anthropogenic sulfate aerosols. *J. Geophys. Res.* **103**, 3815–3823 (1998).
- Andreae, M. O. Aerosols before pollution. *Science* **315**, 50–51 (2007).
- Andreae, M. O. & Rosenfeld, D. Aerosol–cloud–precipitation interactions. Part 1. The nature and sources of cloud-active aerosols. *Earth Sci. Rev.* **89**, 13–41 (2008).
- Penner, J. E., Xu, L. & Wang, M. H. Satellite methods underestimate indirect climate forcing by aerosols. *Proc. Natl Acad. Sci. USA* **108**, 13404–13408 (2011).
- Hoese, C. *et al.* Constraining cloud droplet number concentration in GCMs suppresses the aerosol indirect effect. *Geophys. Res. Lett.* **36**, L12807 (2009).
- Adams, P. J. & Seinfeld, J. H. Predicting global aerosol size distributions in general circulation models. *J. Geophys. Res.* **107**, 4370, doi: 10.1029/2001JD001010 (2002).
- Liu, X., Penner, J. E. & Herzog, M. Global modeling of aerosol dynamics: model description, evaluation, and interactions between sulfate and nonsulfate aerosols. *J. Geophys. Res.* **110**, D18206, doi: 10.1029/2004JD005674 (2005).
- Spracklen, D. V. *et al.* A global off-line model of size-resolved aerosol microphysics. I. Model development and prediction of aerosol properties. *Atmos. Chem. Phys.* **5**, 2227–2252 (2005).
- Mann, G. W. *et al.* Description and evaluation of GLOMAP-mode: a modal global aerosol microphysics model for the UKCA composition-climate model. *Geosci. Model Dev.* **3**, 519–551 (2010).
- Dentener, F. *et al.* Emissions of primary aerosol and precursor gases in the years 2000 and 1750 prescribed data-sets for AeroCom. *Atmos. Chem. Phys.* **6**, 4321–4344 (2006).
- Lee, L. A. *et al.* The magnitude and causes of uncertainty in global model simulations of cloud condensation nuclei. *Atmos. Chem. Phys.* **13**, 8879–8914 (2013).
- Lee, L. A., Carslaw, K. S., Pringle, K. J. & Mann, G. W. Mapping the uncertainty in global CCN using emulation. *Atmos. Chem. Phys.* **12**, 9739–9751 (2012).
- Saltelli, A., Tarantola, S. & Chan, K. P.-S. A quantitative model-independent method for global sensitivity analysis of model output. *Technometrics* **41**, 39–56 (1999).
- Bellouin, N., Quaas, J., Morcrette, J.-J. & Boucher, O. Estimates of aerosol radiative forcing from the MACC re-analysis. *Atmos. Chem. Phys.* **13**, 2045–2062 (2013).
- Woodhouse, M. T. *et al.* Low sensitivity of cloud condensation nuclei to changes in the sea-air flux of dimethyl-sulphide. *Atmos. Chem. Phys.* **10**, 7545–7559 (2010).
- Schmidt, A. *et al.* Importance of tropospheric volcanic aerosol for indirect radiative forcing of climate. *Atmos. Chem. Phys.* **12**, 7321–7339 (2012).
- Otto, A. *et al.* Energy budget constraints on climate response. *Nature Geosci.* **6**, 415–416 (2013).
- Manktelow, P. T., Carslaw, K. S., Mann, G. W. & Spracklen, D. V. Variable CCN formation potential of regional sulfur emissions. *Atmos. Chem. Phys.* **9**, 3253–3259 (2009).
- Penner, J. E., Zhou, C. & Xu, L. Consistent estimates from satellites and models for the first aerosol indirect forcing. *Geophys. Res. Lett.* **39**, L13810 (2012).
- Neelin, J. D., Bracco, A., Luo, H., McWilliams, J. C. & Meyerson, J. E. Considerations for parameter optimization and sensitivity in climate models. *Proc. Natl Acad. Sci. USA* **107**, 21349–21354 (2010).
- Jones, A. *et al.* Indirect sulphate aerosol forcing in a climate model with an interactive sulphur cycle. *J. Geophys. Res.* **106**, 20293–20310 (2001).
- Edwards, J. M. & Slingo, A. Studies with a flexible new radiation code. I. Choosing a configuration for a large scale model. *Q. J. R. Meteorol. Soc.* **122**, 689–719 (1996).
- Rossow, W. B. & Schiffer, R. A. Advances in understanding clouds from ISCCP. *Bull. Am. Meteorol. Soc.* **80**, 2261–2287 (1999).
- Rap, A. *et al.* Natural aerosol direct and indirect radiative effects. *Geophys. Res. Lett.* **40**, 3297–3301 (2013).

**Acknowledgements** This research has received funding from the Natural Environment Research Council AEROS project (project number NE/G006172/1) and GASSP project (project number NE/J024252/1), the EC Seventh Framework Programme under grant agreement FP7-ENV-2010-265148 (Integrated Project PEGASOS), and the National Centre for Atmospheric Science. K.S.C. and P.M.F. are currently Royal Society Wolfson Merit Award holders.

**Author Contributions** K.S.C. wrote the manuscript. L.A.L. did the statistical analysis. C.L.R., K.J.P. and G.W.M. performed the aerosol modelling. M.T.W., L.A.R. and K.J.P. prepared the emissions. K.S.C., L.A.L. and C.L.R. did the data interpretation. A.R. and P.M.F. did the forcing calculations. All authors contributed to the editing of the manuscript.

**Author Information** Reprints and permissions information is available at [www.nature.com/reprints](http://www.nature.com/reprints). The authors declare no competing financial interests. Readers are welcome to comment on the online version of the paper. Correspondence and requests for materials should be addressed to K.S.C. ([k.s.carslaw@leeds.ac.uk](mailto:k.s.carslaw@leeds.ac.uk)).

## METHODS

**Model description.** The GLObal Model of Aerosol Processes (GLOMAP-mode)<sup>15,16</sup> is a three-dimensional global aerosol microphysics model that simulates the evolution of the particle size distribution and size-resolved chemical composition of aerosol particles on a global three-dimensional grid. The model has previously been evaluated against observations<sup>16</sup> and improved by comparing aerosol simulations against a more detailed version of the model that treats the aerosol size distribution using a sectional approach<sup>32</sup>. The GLOMAP models have been widely used and evaluated against global measurements of particle number concentrations<sup>33,34</sup>, CCN<sup>35,36</sup>, aerosol chemical components<sup>37–39</sup>, and cloud droplets<sup>40</sup>. The aerosol module is run within the TOMCAT global three-dimensional offline chemistry transport model<sup>41</sup>. The aerosol and chemical species are transported by three-dimensional meteorological fields read in from the European Centre for Medium-Range Weather Forecasts (ECMWF) ERA-Interim reanalyses for 2008. Aerosol transport is advanced every 30 min by interpolating between the analyses, which are updated every 6 h and the aerosol microphysical/chemical processes are calculated on a range of shorter time-steps of less than 30 min. Uncoupling the aerosol from the model transport and meteorology in the chemistry transport model (so that aerosol does not affect meteorology) is equivalent to the commonly used “double-call” approach in a climate model<sup>42</sup> in which the aerosol radiative effects are decoupled from the model physics so that particular radiative forcings can be diagnosed using pairs of model runs. The model was run at a horizontal resolution of  $2.8^\circ \times 2.8^\circ$  with 31 vertical levels between the surface and 10 hPa.

The aerosol size distribution is defined by seven log-normal modes: one nucleation mode and soluble and insoluble modes covering the Aitken, accumulation and coarse size ranges. The aerosol chemical components are sulphate, sea salt, black carbon, particulate organic matter and dust. Secondary organic aerosol is produced from the first stage oxidation products of biogenic monoterpenes and anthropogenic volatile-organic-carbon compounds, and is assumed to have zero vapour pressure. It is combined with the particulate-organic-matter component after kinetic condensation on the aerosol. The model includes dust emissions, but we do not perturb them because we focus on the effect on CCN concentrations, which we have previously shown are not strongly affected by dust particles even in intense dust storms<sup>43</sup>.

The microphysical model resolves the main processes that shape the particle size distribution on a global scale: new particle formation, coagulation, gas-to-particle transfer, cloud processing, and dry and wet deposition. Wet deposition of particles occurs by two processes. In-cloud nucleation scavenging in which activated particles form cloud droplets and are removed in precipitation and below-cloud impaction scavenging by falling raindrops. ECMWF meteorological fields are used to diagnose large-scale frontal precipitation and sub-grid convective precipitation is assumed to occur in 30% of the affected grid box area. Low-level stratiform clouds are read in separately from International Satellite Cloud Climatology Project (ISCCP) D2 data<sup>30</sup>. In these clouds we assume that aerosol particles are activated and subsequently undergo ‘cloud processing’ in which sulphate mass is added to activated aerosol owing to the aqueous-phase oxidation of sulphur dioxide.

Concentrations of the oxidants OH, O<sub>3</sub>, H<sub>2</sub>O<sub>2</sub> and NO<sub>3</sub> and HO<sub>2</sub> were specified on the three-dimensional grid using six-hourly monthly mean concentrations from a TOMCAT simulation with detailed tropospheric chemistry<sup>44</sup>. Concentrations of H<sub>2</sub>O<sub>2</sub> are depleted through the aqueous-phase reaction with SO<sub>2</sub> and replenished through the reaction HO<sub>2</sub> + HO<sub>2</sub> (ref. 15). A spin-up period of six months was performed (three months of which had parameters set at their median value and formed the basis of a further three-month spin for each of the runs with the changed parameter settings).

**Emissions.** The emission fluxes were perturbed by scaling baseline values, which are specified in Extended Data Table 1 for the 1750–2000 simulations, and in Extended Data Table 2 for the 1850–2000, 1900–2000 and 1850–1980 simulations. The Aerosol Comparisons between Observations and Models (AeroCom) emissions scenarios used for 1750 and 2000 are not available for the intermediate years. For the three additional time periods we therefore used the emissions prepared for the Atmospheric Chemistry and Climate Model Intercomparison Project (ACCMIP<sup>45</sup>) for 1850, 1900, 1980 and 2000. For the sensitivity runs, we show results for June after two months of spin-up after the perturbations were applied.

**Cloud droplet number concentrations.** CDNCs were calculated as a post-processing step using an activation parameterization<sup>46</sup> and the modelled monthly mean aerosol size distribution and composition in each grid cell for each perturbed parameter run. These calculations account for the coupling between the uncertain aerosol particle size distribution (and composition) and the number of particles activated into cloud droplets.

An updraught speed of  $0.15 \text{ m s}^{-1}$  was used over marine regions and  $0.3 \text{ m s}^{-1}$  over land, which is typical of cloud-base speeds in low-level stratus and stratocumulus clouds. Because updraft is highly variable in clouds it is normal to report updraft measurements as the standard deviation  $\sigma$  of a probability density function

of updrafts (normally centred on zero). However, it is possible to calculate CDNC using a single characteristic updraft speed ( $w^*$ ) that gives comparable results to using a probability density function of updrafts<sup>47</sup>. The characteristic speed is given by  $w^* = B\sigma$ , where  $B$  is a conversion factor constrained through closure studies to be in the range 0.65–0.8 (refs 47, 48). Here, we use  $w^* = 0.15 \text{ m s}^{-1}$  over marine regions, which equates to  $\sigma = 0.19\text{--}0.23 \text{ m s}^{-1}$ , and  $w^* = 0.3 \text{ m s}^{-1}$  over land, which equates to  $\sigma = 0.38\text{--}0.46 \text{ m s}^{-1}$ . The updrafts used to calculate CDNC should be representative of cloud base, where activation primarily occurs. Updrafts at cloud base are typically smaller than in-cloud updrafts as the latent heat released by condensation onto cloud droplets fuels higher in-cloud updrafts<sup>49,50</sup>. For example, in measurements during the Marine Stratus/Stratocumulus Experiment (MASE) experiment<sup>51</sup> the standard deviation rises from  $0.3 \text{ m s}^{-1}$  at cloud base to  $0.6 \text{ m s}^{-1}$  at cloud top. Thus, we consider our updraft velocities to be appropriate for cloud base.

To test the effect of higher updraft speeds, we recalculated CDNC for July using  $w^* = 0.25 \text{ m s}^{-1}$  over oceans and  $0.4 \text{ m s}^{-1}$  over land. We then built a new emulator for global annual mean forcing. The global mean forcing changes negligibly at the higher speeds. The fractional contributions to variance change from low to high updraft speed as follows: natural aerosol changes from 45% to 42%, anthropogenic emissions decrease from 34% to 33% and processes rise from 19% to 21%.

**Radiative forcing.** The forcing was calculated as the difference of top-of-the-atmosphere net short-wave plus long-wave radiative fluxes between the PD and the PI periods. The PD and PI runs were performed using identical meteorological analyses. Each parameter perturbation run in the PI period was paired with its equivalent setting in the PD period. The PI and PD simulations are therefore identical in every respect except for the anthropogenic emissions. The modelled aerosol properties were then used to calculate the CDNC values in the PI and PD periods, from which the forcing was calculated for each two-dimensional grid point of the model.

We used the off-line version of the Edwards and Slingo radiative transfer model<sup>29</sup> with six bands in the short-wave and nine bands in the long-wave, with a delta-Eddington two-stream scattering solver at all wavelengths. We used a monthly mean climatology for water vapour, temperature and ozone based on ECMWF reanalysis data, together with surface albedo and cloud optical depth fields from the International Satellite Cloud Climatology Project (ISCCP-D2)<sup>30</sup> for the year 2000. The diurnal cycle of incoming solar radiation was accounted for, but no diurnal cycle of cloud cover was assumed. The sensitivity of our forcing estimates to the cloud climatology is very small<sup>31</sup>, according to an extra set of calculations performed using the 1983–2008 multi-annual ISCCP cloud climatology.

The cloud albedo forcing between the PI and PD experiments is quantified by modifying the cloud droplet effective radius  $r_e$  for low- and mid-level water clouds up to 600 hPa:

$$r_e^{\text{PI}} = r_e^{\text{PD}} \times \left( \frac{\text{CDNC}^{\text{PD}}}{\text{CDNC}^{\text{PI}}} \right)^{1/3}$$

where CDNC is the monthly mean cloud droplet number concentration in each grid cell. A fixed value for  $r_e^{\text{PD}} = 10 \mu\text{m}$  is used in order to ensure consistency with the ISCCP cloud retrievals. This overestimates the strength of the forcing because clouds with more droplets tend, on average, to have less water for reasons that are physically understood<sup>52</sup>. However, our conclusions about the relative sources of uncertainty are not affected.

**Perturbed parameters.** The ensemble of model runs was designed to enable an emulator to be built. The ensemble consists of 168 combinations of parameter settings from 28 parameters representing aerosol and precursor gas emissions, microphysical processes and aerosol model structures. The uncertainty range for each parameter was chosen based on expert elicitation<sup>18</sup> (see Extended Data Table 3 for a complete list). Parameter combinations within the uncertainty range were defined by a maximin Latin Hypercube sampling of the parameter space. Paired simulations were run for one year for 1750 and 2000 using the AeroCom emissions (336 runs in total) and for one month for 1850, 1900, 1980 and 2000 using the ACCMIP emissions. Each parameter setting in the PI era was paired with the same parameter setting in the PD. Anthropogenic emissions (from fossil fuel, biofuel and biomass burning) were set to their 1750, 1850 or 1900 values in the PI era and the year 1980 and 2000 values for the PD and were perturbed by the same factor.

Parameters 1 to 14 define aerosol microphysical processes and the definition of the size distribution modal parameters, whereas parameters 15 to 28 define the emission of aerosols and precursor gases. Full details about the parameter ranges and the process of expert elicitation are provided in ref. 18. Here we summarize the main aspects of the perturbed parameters.

The boundary-layer nucleation parameterization (P1) assumes a rate  $j = A[\text{H}_2\text{SO}_4(\text{g})]$ , with  $A$  (in units of  $\text{s}^{-1}$ ) being the perturbed parameter. Throughout the atmosphere (but important only in the free troposphere) we use a binary homogeneous  $\text{H}_2\text{SO}_4\text{--H}_2\text{O}$  nucleation rate model scaled by an uncertain factor (P2).

Ageing is the process by which freshly emitted carbonaceous particles (for example, from biomass burning) can become increasingly water soluble as they accumulate water-soluble compounds during transport. The controlling parameter, as used in many global models<sup>53</sup>, is the number of monolayers of soluble material required to convert the particles into water-soluble particles, which can then act as CCN. The lower limit of our assumed ageing means that initially insoluble particles become soluble on the timescale of hours in polluted regions. This process affects the number of aerosol particles able to form cloud droplets in the forcing calculation, and also affects the cloud processing of aerosol during run time of the model.

The activation diameter (P4) defines the dry-equivalent diameter at which particles are able to activate to cloud droplets during run time of the model. A single value of activation diameter is used globally in a given run. The activation diameter controls the formation of cloud droplets in all low-level clouds, and thereby controls which particles undergo cloud processing (sulphate production on the particles due to oxidation of sulphur dioxide) and removal in precipitation, and therefore shapes the particle size distribution. Cloud droplet concentrations from run-time of the model are not used in the forcing calculations (they are only used as a physical process that shapes the particle size distribution). For the forcing (see previous section) cloud droplet concentrations are quantified as a post-processing step based on the uncertain particle size distributions and an assumed updraft speed. In reality, the activation diameter in a given cloud updraft is controlled by the particle size distribution, solubility and updraft speed. The updraft speed was not included as a perturbed parameter because the chemical transport model does not have a parameterization of updrafts in different cloud types and environments. Perturbation of the activation diameter accounts approximately for the uncertainty in updraft speed, but by prescribing a value in each simulation it ignores the way that the diameter is coupled to the properties of the aerosol size distribution in a given grid cell. This approach is likely to overestimate the uncertainty because it allows a larger variation in the number of aerosol particles that can be cloud processed, which would otherwise be damped by the coupling of particle number and activation diameter. Nevertheless, activation diameter makes a small contribution to global forcing uncertainty (Fig. 2c).

The parameters SO2O3\_CLEAN and SO2O3\_POLL (P5 and P6) control the cloud droplet pH, which affects the production rate of aerosol sulphate from oxidation of sulphur dioxide by ozone. The pH is the perturbed parameter and can cause a change in rate by a factor of  $10^5$  for pH between 3 and 6. One parameter is used for clean (lower acidity) environments (sulphur dioxide less than 0.5 parts per billion) and one for polluted environments.

The in-cloud scavenging diameter offset (P7) controls the diameter of aerosols that can be removed by in-cloud nucleation scavenging. This allows some particles to be activated but not scavenged, assuming that the largest droplets initiate precipitation. The lower limit of P7 (zero nanometres) assumes all activated particles are subject to removal during precipitation.

The scavenging efficiency in ice-containing clouds (P8) controls the fraction of particles accessible to nucleation scavenging when air is below  $-10^\circ\text{C}$ . Our previous work has shown this parameter to be important in controlling aerosol transport to the Arctic<sup>38</sup>. Dry deposition of Aitken and accumulation mode particles (P9 and P10) is scaled for each particle size by a given factor. GLOMAP calculates the wind speed and size-dependent deposition velocity due to Brownian diffusion, impaction and interception. The accumulation and Aitken mode width parameters (P11 and P12) define prescribed, globally constant geometric standard deviations of the log-normal size distribution modes. The mode separation diameters (P13 and P14) define the ranges over which the geometric mean radius can vary while staying in a particular mode.

Fossil fuel, biofuel and biomass burning particle emission flux parameters (P15, P16 and P17) scale the mass emission fluxes in the PI based on the 1750, 1850 or 1900 emissions and in the PD based on the year 2000 emissions. The spatial distribution of emissions is different in the PI and PD. Our perturbation accounts for uncertainty in the monthly mean flux but does not account for uncertainty in the spatial pattern or temporal variability in the emissions. Thus, for wildfires we are not able to separate the effects of more intense fires versus more frequent fires, which might have different effects on forcing uncertainty. The biomass burning from open fires was not separated into natural and anthropogenic emissions, so we cannot apportion the uncertainty. Examination of the variation of uncertainty due to these parameters shows a clear seasonal cycle, with a peak contribution to global mean variance of 5% in July and August, which can be attributed to northern mid-latitude wildfires, versus generally less than 1% at other times. The tropical fires are important for CCN<sup>18</sup> but the uncertainty in forcing is limited by the low sensitivity of cloud albedo at very high CCN concentrations. Because most of the northern mid-latitude emissions can be associated with natural fires<sup>54</sup>, we have associated the biomass burning uncertainties with the natural emissions.

Fossil fuel, biofuel and biomass burning particle emission sizes (P18, P19 and P20) directly control the number of emitted particles for a given mass flux, and therefore directly influence the CCN population. The sub-grid scale sulphate particle production parameters (P21 and P22) define the formation of particles in sub-grid scale power plant plumes<sup>55,56</sup>. P21 defines the fraction of the emitted sulphur dioxide mass that enters the model grid square as new sulphate particles and P22 defines the dry size of these particles (and hence their number concentration for fixed mass) when emitted into the global grid box.

The sea spray particle mass flux (P23) is scaled by a factor. GLOMAP-mode simulates sea spray particles between 35 nm and 20  $\mu\text{m}$  dry diameter. This parameter conflates multiple sources of uncertainty associated with the wind-speed dependence of the flux such as processes not unaccounted for in the parameterizations (for example, fetch), the wind speed, and the limited spatial resolution of the wind fields in the model.

Anthropogenic sulphur dioxide emissions (P24) are scaled by a factor based on the emissions in 1750, 1850, 1900 and 2000, as described above. Continuously degassing volcanic sulphur dioxide emissions (P25) are scaled based on a global inventory widely used in global models<sup>57</sup>. Time-averaged sporadic emissions are also included. Volcanic emissions are assumed to be the same in the PI and PD simulations.

DMS emissions (P26) are controlled by the sea-water concentration of DMS<sup>58</sup> and the wind-driven transfer velocity parameterization<sup>59</sup>. We conflate these uncertainties by perturbing the calculated sea-air transfer flux by a given factor. This leads to identical absolute perturbations to the DMS flux in the PI era and the PD. We do not account for uncertainty in the spatial pattern of DMS seawater concentration, which is likely to be an important factor in the overall uncertainty<sup>60</sup>.

The biogenic secondary-organic-aerosol production parameter (P27) conflates the uncertainty in the emissions of the precursor gases (biogenic volatile organic carbons) and the uncertainty in the yield of secondary-organic-aerosol material following oxidation reactions into a single parameter. P27 scales the volatile organic carbon emissions (with fixed chemical yield) such that global annual secondary-organic-aerosol production lies between the values given in the table. There are also uncertainties in the volatility of different compounds that we do not account for here. The range of emissions used here has been shown to span the range of global *in situ* measurements of organic aerosol<sup>37</sup>.

Anthropogenic secondary organic aerosol production (P28) is treated in a similar way to biogenic secondary organic aerosol, by conflating the uncertainty in emissions and yield into a single emission uncertainty. We used the same approach as in ref. 37 by scaling gridded carbon monoxide emissions over a range known to span the range of observed organic aerosol in the PD atmosphere. The range is then scaled further to account for the changes in carbon monoxide emissions in 1850, 1900 and 1980.

**Model emulation.** Gaussian process emulation<sup>18–20</sup> was used to estimate model predictions at untried points throughout the space of the uncertain model parameters. An emulator was built for the monthly mean first indirect radiative forcing for every two-dimensional grid point (to produce Fig. 1 in the main text) and for the global annual mean and monthly mean forcings to generate Fig. 2 in the main text. The emulator was validated in each case using 84 additional model runs (Extended Data Fig. 1) to ensure that the emulator uncertainty around its mean is low compared to the parametric uncertainty. Twenty-eight of the validation runs were designed to lie near the training points and 64 were defined using a separate Latin Hypercube design<sup>61</sup>. The coefficient of determination ( $r^2$ ) of the global annual mean emulator forcing versus simulated forcing is 0.94.

**Variance-based sensitivity analysis.** Variance-based sensitivity analysis is used to decompose the uncertainty in the model predictions to the uncertainty in the model parameters. The total variance of the forcing was calculated by sampling from the emulator mean function using the extended-FAST method<sup>20</sup>. We sampled 5,000 points per parameter (140,000 in total) from the emulator to obtain a probability distribution of forcing. Two measures of sensitivity were calculated: the main effect index measures by how much the variance will be reduced if the parameter can be learnt precisely, and the total effect index measures both the individual effect and the interaction effect of each parameter with all others. The two sensitivity measures are compared to assess the sensitivity of the model output to interactions. Figure 2b (see main text) shows that parameter interactions account for generally less than 10% of the monthly global mean forcing variance (shown as the residual white space above each coloured bar). We note that a nonlinear response of the model output to a parameter across the specified range is accounted for in the main effect variance.

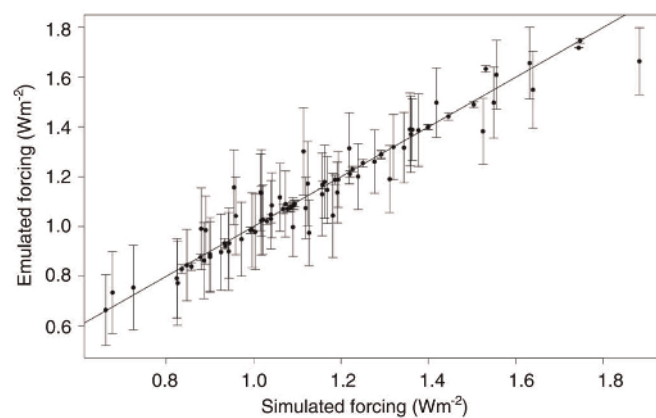
**Uncertainty results using different reference periods.** Extended Data Table 4 presents results for the additional simulations in which alternative reference years were used for the calculation of forcing (1850 and 1900 instead of 1750), as well as for the period 1850–1980.

32. Mann, G. W. *et al.* Intercomparison of modal and sectional aerosol microphysics representations within the same 3-D global chemical transport model. *Atmos. Chem. Phys.* **12**, 4449–4476 (2012).



33. Spracklen, D. V. *et al.* Explaining global surface aerosol number concentrations in terms of primary emissions and particle formation. *Atmos. Chem. Phys.* **10**, 4775–4793 (2010).
34. Reddington, C. L. *et al.* Primary versus secondary contributions to particle number concentrations in the European boundary layer. *Atmos. Chem. Phys.* **11**, 12007–12036 (2011).
35. Korhonen, H. *et al.* Influence of oceanic dimethyl sulfide emissions on cloud condensation nuclei concentrations and seasonality over the remote Southern Hemisphere oceans: a global model study. *J. Geophys. Res.* **113**, D15204 (2008).
36. Spracklen, D. V., Carslaw, K. S., Poschl, U., Rap, A. & Forster, P. M. Global cloud condensation nuclei influenced by carbonaceous combustion aerosol. *Atmos. Chem. Phys.* **11**, 9067–9087 (2011).
37. Spracklen, D. V. *et al.* Aerosol mass spectrometer constraint on the global secondary organic aerosol budget. *Atmos. Chem. Phys.* **11**, 12109–12136 (2011).
38. Browne, J., Carslaw, K. S., Arnold, S. R., Pringle, K. & Boucher, O. The scavenging processes controlling the seasonal cycle in Arctic sulphate and black carbon aerosol. *Atmos. Chem. Phys.* **12**, 6775–6798 (2012).
39. Schmidt, A. *et al.* Excess mortality in Europe following a future Laki-style Icelandic eruption. *Proc. Natl Acad. Sci. USA* **108**, 15710–15715 (2011).
40. Pringle, K. J. *et al.* A multi-model assessment of the impact of sea spray geoengineering on cloud droplet number. *Atmos. Chem. Phys.* **12**, 11647–11663 (2012).
41. Chipperfield, M. P. New version of the TOMCAT/SIMCAT off-line chemical transport model: intercomparison of stratospheric tracer experiments. *Q. J. R. Meteorol. Soc.* **132**, 1179–1203 (2006).
42. Bellouin, N. *et al.* Impact of the modal aerosol scheme GLOMAP-mode on aerosol forcing in the Hadley Centre Global Environmental Model. *Atmos. Chem. Phys.* **13**, 3027–3044 (2013).
43. Manktelow, P. T., Carslaw, K. S., Mann, G. W. & Spracklen, D. V. The impact of dust on sulfate aerosol, CN and CCN during an East Asian dust storm. *Atmos. Chem. Phys.* **10**, 365–382 (2010).
44. Arnold, S. R., Chipperfield, M. P. & Blitz, M. A. A three-dimensional model study of the effect of new temperature-dependent quantum yields for acetone photolysis. *J. Geophys. Res.* **110**, D22305, doi: 10.1029/2005JD005998 (2005).
45. Lamarque, J.-F. *et al.* Historical (1850–2000) gridded anthropogenic and biomass burning emissions of reactive gases and aerosols: methodology and application. *Atmos. Chem. Phys.* **10**, 7017–7039 (2010).
46. Fountoukis, C. & Nenes, A. Continued development of a cloud droplet formation parameterization for global climate models. *J. Geophys. Res.* **110**, D11212 (2005).
47. Morales, R. & Nenes, A. Characteristic updrafts for computing distribution-averaged cloud droplet number, autoconversion rate and effective radius. *J. Geophys. Res.* **115**, D18220, doi: 10.1029/2009JD013233 (2010).
48. Peng, Y., Lohmann, U. & Leaitch, R. Importance of vertical velocity variations in cloud droplet nucleation process of marine stratus clouds. *J. Geophys. Res. Atmos.* **110**, D21213, doi:10.1029/2004JD004922 (2005).
49. Lu, M. & Seinfeld, J. H. Study of the aerosol indirect effect by large-eddy simulation of marine stratocumulus. *J. Atmos. Sci.* **62**, 3909–3932 (2005).
50. Hill, A. A., Feingold, G. & Jiang, H. The influence of entrainment and mixing assumption on aerosol-cloud interactions in marine stratocumulus. *J. Atmos. Sci.* **66**, 1450–1464 (2009).
51. Guo, H., Liu, Y. & Daum, P. H. Senum, G. I. & Tao, W.-K. Characteristics of vertical velocity in marine stratocumulus: comparison of large eddy simulations with observations. *Environ. Res. Lett.* **3**, 045020 (2008).
52. Ackerman, A. S. *et al.* The impact of humidity above stratiform clouds on indirect climate forcing. *Nature* **432**, 1014–1017 (2004).
53. Wilson, J., Cuvelier, C. & Raes, F. A modeling study of global mixed aerosol fields. *J. Geophys. Res.* **106**, 34081–34092 (2001).
54. Stocks, B. J. *et al.* Large forest fires in Canada, 1959–1997. *J. Geophys. Res.* **107**, 8149, doi: 10.1029/2001JD000484 (2002).
55. Luo, G. & Yu, F. Sensitivity of global cloud condensation nuclei concentrations to primary sulfate emission parameterizations. *Atmos. Chem. Phys.* **11**, 1949–1959 (2011).
56. Stevens, R. G. *et al.* Nucleation and growth of sulfate aerosol in coal-fired power plant plumes: sensitivity to background aerosol and meteorology. *Atmos. Chem. Phys.* **12**, 189–206 (2012).
57. Andres, R. J. & Kasgnoc, A. D. A time-averaged inventory of subaerial volcanic sulfur emissions. *J. Geophys. Res.* **103**, 25251–25262 (1998).
58. Kettle, A. J. & Andreae, M. O. Flux of dimethylsulfide from the oceans: a comparison of updated data sets and flux models. *J. Geophys. Res.* **105**, 26793–26808 (2000).
59. Nightingale, P. D. *et al.* In situ evaluation of air-sea gas exchange parameterizations using novel conservative and volatile tracers. *Glob. Biogeochem. Cycles* **14**, 373–387 (2000).
60. Woodhouse, M. T. *et al.* Sensitivity of cloud condensation nuclei to regional changes in dimethyl-sulphide emissions. *Atmos. Chem. Phys.* **13**, 2723–2733 (2013).
61. Bastos, L. & O'Hagan, A. Diagnostics for Gaussian process emulators. *Technometrics* **4**, 425–438 (2011).
62. Cofala, J., Amann, M., Klimont, Z. & Schopp, W. *Scenarios of World Anthropogenic Emissions of SO<sub>2</sub>, NO<sub>x</sub> and CO up to 2030*. Internal report of the Transboundary Air Pollution Programme (International Institute for Applied Systems Analysis, Laxenburg, 2005).
63. Bond, T. C. *et al.* A technology-based global inventory of black and organic carbon emissions from combustion. *J. Geophys. Res.* **109**, D14203, doi:10.1029/2003JD003697 (2004).
64. van der Werf, G. R., Randerson, J. T., Collatz, G. J. & Giglio, L. Carbon emissions from fires in tropical and subtropical ecosystems. *Glob. Change Biol.* **9**, 547–562 (2003).
65. Gong, S. A parameterization of sea-salt aerosol source function for sub and super-micron particles. *Glob. Biogeochem. Cycles* **17**, 1097, doi: 10.1029/2003GB002079 (2003).
66. Guenther, A. *et al.* A global model of natural volatile organic compound emissions. *J. Geophys. Res.* **100**, 8873–8892 (1995).





**Extended Data Figure 1 | Validation of the global annual mean forcing emulator.** The error bars show the emulator 95% uncertainty range around the mean prediction. The 1:1 line is shown.

Extended Data Table 1 | Emissions of aerosols and precursor gases used in the 1750–2000 simulations

Aerosol source	Emitted species	PD (2000) flux	PI (1750) flux	Ref.
Fossil fuel	BC / Tg C per year	3.0	0.0	17
	POM / Tg POM per year	3.2	0.0	17
Power stations	SO <sub>2</sub> / Tg S per year	24.2	0.0	17, 62
Industrial processes	SO <sub>2</sub>	19.6	0.0	17, 62
Transportation	SO <sub>2</sub>	4.8	0.0	17, 62
Off-road	SO <sub>2</sub>	0.8	0.0	17, 62
Biofuel	BC / Tg C per year	1.6	0.4	17, 63
	POM / Tg POM per year	9.1	1.6	17, 63
Domestic	SO <sub>2</sub> / Tg S per year	4.8	0.12	17, 63
Wildfires	BC / Tg C per year	3.1	1.03	17, 64
	POM / Tg POM per year	34.7	12.8	17, 64
	SO <sub>2</sub> / Tg S per year	2.1	1.46	17, 64
Volcanoes	SO <sub>2</sub> / Tg S per year	12.6	12.6	57
Marine dimethyl sulphide	DMS* / Tg S per year	17.1	17.1	58
Sea spray	Salt	Wind-dependent flux	Wind-dependent flux	65
Biogenic volatile organic carbon	Monoterpenes ( $\alpha$ -pinene) / Tg POM produced per year	5-360	5-360	37, 66 (for spatial/temporal variation)
Anthropogenic volatile organic carbon	VOC / Tg POM produced per year	2-112	0.0	37

\* The DMS emission flux is a global annual value but emissions are calculated at each time step based on the seawater DMS concentration field<sup>58</sup> and a sea–air transfer velocity<sup>59</sup>. These baseline emissions were perturbed according to the factors given in Extended Data Table 3, except for the volatile organic carbon emissions, which were perturbed over the absolute range indicated in this table and in Extended Data Table 3. BC, black carbon; POM, particulate organic matter; VOC, volatile organic carbon.

Extended Data Table 2 | Emissions of aerosols and precursor gases used in the 1850–2000, 1900–2000 and 1850–1980 simulations.

Aerosol source	Emitted species	2000 flux	1980 flux	1900 flux	1850 flux	Ref.
Fossil fuel	BC / Tg C per year	3.0	2.1	0.4	0.1	45
	POM / Tg POM per year	5.8	3.5	0.8	0.2	45
Power stations	SO <sub>2</sub> / Tg S per year	24.8	30.7	1.8	0.0	45
Industrial processes	SO <sub>2</sub>	8.8	11.3	5.6	0.6	45
Transportation	SO <sub>2</sub>	7.7	6.9	0.9	0.0	45
Off-road	SO <sub>2</sub>	5.6	3.6	0.9	0.0	45
Biofuel	BC / Tg C per year	2.2	2.5	2.0	1.0	45
	POM / Tg POM per year	12.1	12.0	8.9	6.4	45
Domestic	SO <sub>2</sub> / Tg S per year	4.3	6.2	2.6	0.4	45
Wildfires	BC / Tg C per year	1.03	1.03	1.03	1.03	17, 64
	POM / Tg POM per year	12.8	12.8	12.8	12.8	17, 64
	SO <sub>2</sub> / Tg S per year	1.46	1.46	1.46	1.46	17, 64
Volcanoes	SO <sub>2</sub> / Tg S per year	12.6	12.6	12.6	12.6	57
Marine dimethyl sulphide	DMS / Tg S per year	17.1	17.1	17.1	17.1	58
Sea spray	Salt	Wind-dependent flux	Wind-dependent flux	Wind-dependent flux	Wind-dependent flux	65
Biogenic volatile organic carbon	Monoterpenes ( $\alpha$ -pinene) / Tg POM produced per year	5-360	5-360	5-360	5-360	37, 66
Anthropogenic volatile organic carbon	VOC / Tg POM produced per year	2.7-145.0	2.6-150.0	0.5-26.5	0.3-15.0	37, 45 (CO emissions)



Extended Data Table 3 | Parameters and their maximum ranges used in the model simulations.

Parameter number	Parameter name	Description	Uncertainty range	Effect
<b>Process parameters</b>				
P1	BL_NUC	Boundary layer nucleation rate	$3.2 \times 10^{-7} - 2 \times 10^{-4} \text{ s}^{-1}$	Absolute
P2	FT_NUC	Free troposphere nucleation rate	0.01 – 10	Scaled
P3	AGEING	Ageing 'rate' from insoluble to soluble	0.3 – 5 monolayer	Absolute
P4	ACT_DIAM	Cloud drop activation dry diameter	50 – 100 nm	Absolute
P5	SO2O3_CLEAN	pH of cloud drops (controls $\text{SO}_2 + \text{O}_3$ )	pH 4 – 6.5	Absolute
P6	SO2O3_POLL	pH of cloud drops ( $\text{SO}_2 + \text{O}_3$ )	pH 3.5 – 5	Absolute
P7	NUC_SCAV_DIAM	Nucleation scavenging offset dry diameter	0 – 50 nm	Absolute
P8	NUC_SCAV_ICE	Nucleation scavenging fraction (accumulation mode) in mixed and ice clouds ( $T < -15^\circ \text{C}$ )	0 – 1	Scaled
P9	DRYDEP_AIT	Dry deposition velocity of Aitken mode aerosol	0.5 – 2	Scaled
P10	DRYDEP_ACC	Dry deposition velocity of accumulation mode aerosol	0.1 – 10	Scaled
P11	ACC_WIDTH	Mode width (accumulation soluble/insoluble mode)	1.2 – 1.8	Absolute
P12	AIT_WIDTH	Mode width (Aitken soluble/insoluble)	1.2 – 1.8	Absolute
P13	NUC-AIT_SEP	Mode separation diameter (nucleation/Aitken)	9 – 18 nm	Absolute
P14	AIT-ACC_SEP	Mode separation diameter (Aitken/accumulation)	0.9 – $2 \times \text{ACT\_DIAM}$	Scaled
<b>Aerosol and precursor gas emissions</b>				
P15	FF_EMS	BCOC mass emission rate (fossil fuel)	0.5 – 2	Scaled
P16	BB_EMS	BCOC mass emission rate (biomass burning)	0.25 – 4	Scaled
P17	BF_EMS	BCOC mass emission rate (biofuel)	0.25 – 4	Scaled
P18	FF_DIAM	BCOC emitted number median dry diameter (fossil fuel)	30 – 80 nm	Absolute
P19	BB_DIAM	BCOC emitted number median dry diameter (biomass burning)	50 – 200 nm	Absolute
P20	BF_DIAM	BCOC emitted number median dry diameter (biofuel)	50 – 200 nm	Absolute
P21	PRIM_SO4_FRAC	Mass fraction of $\text{SO}_2$ converted to new sulphate particles in sub-grid plumes	0 – 1%	Scaled
P22	PRIM_SO4_DIAM	Emitted number median dry diameter of sub-grid sulphate particles	20 – 100 nm	Absolute
P23	SEASPRAY	Sea spray mass flux (coarse/accumulation)	0.2 – 5	Scaled
P24	ANTH_SO2	$\text{SO}_2$ emission flux (anthropogenic)	0.6 – 1.5	Scaled
P25	VOLC_SO2	$\text{SO}_2$ emission flux (volcanic)	0.5 – 2	Scaled
P26	DMS_FLUX	DMS emission flux	0.5 – 2	Scaled
P27	BIO_SOA	Biogenic monoterpene production of SOA	5 – 360 Tg POM per year *	Absolute
P28	ANTH_SOA	Anthropogenic VOC production of SOA	2 – 112 Tg POM per year *	Absolute

The Latin Hypercube sampling of parameter combinations was designed to lie within these ranges. In the 'effect' column, for the scaled parameters the magnitude of the parameter was multiplied by a factor lying between the maximum and minimum given in the 'uncertainty range' column and for absolute adjustments, the parameter was set to a value within the range of absolute values in the 'uncertainty range' column. BCOC, black carbon/organic carbon; SOA, secondary organic aerosol. \*The values given refer to the mass of POM produced, although the perturbations were actually applied to the emitted VOCs. The POM range refers to year 2000. For other years see Extended Data Table 2. The baseline emissions are given in Extended Data Tables 1 and 2.

**Extended Data Table 4 | Results for the different periods.**

Period	Emissions	Forcing (W m <sup>-2</sup> )	Forcing standard deviation (W m <sup>-2</sup> )	Forcing standard deviation divided by forcing	Percentage of variance due to natural emissions	Percentage of variance due to anthropogenic emissions	Percentage of variance due to aerosol processes
Annual mean values							
1750–2000	AeroCom	−1.16	0.22	0.18	45	34	14
June mean values							
1750–2000	AeroCom	−1.42	0.27	0.19	45	38	13
1850–2000	ACCMIP	−1.30	0.28	0.22	37	46	11
1900–2000	ACCMIP	−0.96	0.20	0.21	37	43	13
1850–1980	ACCMIP	−1.29	0.27	0.21	38	47	11

All numbers refer to global means. The last three columns refer to percentage of variance.